Engineering Fracture Mechanics 313 (2025) 110664

Contents lists available at ScienceDirect

Engineering Fracture Mechanics

journal homepage: www.elsevier.com/locate/engfracmech

The relationship between crack front twisting, plastic zone and $da/dN - \Delta K$ curve of fatigue cracks in AA2024-T3

Vanessa Schöne *, Florian Paysan, Eric Breitbarth

Institute of Materials Research, German Aerospace Center (DLR), Köln, Germany

ARTICLE INFO

Keywords:
Plastic zone
Fracture surface
Digital image correlation
Microscopy
Fatigue crack growth

ABSTRACT

While fatigue crack growth is inherently a three-dimensional challenge, it is often modelled in two dimensions for simplicity. This study explores the relationship between the two-dimensional primary plastic zone (PPZ) on the surface of specimens and the three-dimensional twisting of the crack front leading to a slanted crack front. Fatigue crack growth experiments were conducted using 2-mm-thick MT-160 AA2024-T3 sheet specimens in both L-T and T-L crack orientations. High-resolution digital image correlation (HR-DIC) was employed to capture the PPZ within the surface displacement data and correlate its morphology with the twisting angle of the slanted crack front.

Further, this study investigates how the twisting of the crack front affects the crack propagation curve, represented as $da/dN - \Delta K$, by examining its influence on the mixed-mode I/II/III loading state along the crack front. Here, we utilize finite element simulations to derive a mapping function that adjusts ΔK to ΔK_{eqv}, accounting for the twisted crack front caused mixed-mode loading conditions. The modified $da/dN - \Delta K_{eqv}$ curves for both L-T and T-L orientations demonstrated similar behaviour, suggesting that differences in their crack front twisting may explain the discrepancies observed in their traditional $da/dN - \Delta K$ crack propagation curves.

1. Introduction

Fatigue crack growth is strongly correlated to a number of interrelated aspects, including the loading conditions, the characteristics of the crack tip field, the plastic zone at the crack tip, the microstructure of the material and the shape of the fracture surface [2,3]. Understanding these mechanisms and their interactions with environmental factors, loading conditions, and the material's microstructure [2], is crucial for developing more accurate crack propagation models that are based on a physical foundation to enhance service life predictions [4].

The plastic zone (PZ) ahead of the crack tip represents the crack tip loading condition during fatigue crack growth in ductile materials. Two types of PZ can be distinguished under cyclic loading conditions: The primary plastic zone (PPZ) includes all the deformed material near the crack tip. In contrast, the cyclic plastic zone (CPZ) includes all material with cyclic plastic deformation within a load cycle. Irwin introduced Eq. (1) as an estimate for the size of the PPZ, r_{ppz}, primarily influenced by the maximum stress intensity factor, K_{max}, and the yield strength of the material, σ_y.

$$r_{ppz} = \frac{1}{\pi}\left(\frac{K_{max}}{\sigma_{yield}}\right)^2 \tag{1}$$

* Corresponding author.
E-mail address: vanessa.schoene@dlr.de (V. Schöne).

https://doi.org/10.1016/j.engfracmech.2024.110664
Received 18 September 2024; Received in revised form 11 November 2024; Accepted 14 November 2024

Available online 22 November 2024

Nomenclature

Δa	Crack growth increment [mm]
ΔA_{pz}	Plastic zone wing area difference [mm^2]
ΔK	Cyclic stress intensity factor [MPa$\sqrt{m}$]
$\Delta K_{equ,corr}$	Cyclic corrected equivalent stress intensity factor [MPa$\sqrt{m}$]
ΔK_{equ}	Cyclic equivalent stress intensity factor [MPa$\sqrt{m}$]
$\Delta K_{I,ASTM}$	Cyclic Mode I stress intensity factor according to [1] [MPa$\sqrt{m}$]
$\Delta K_{I,corr}$	Cyclic corrected Mode I stress intensity factor [MPa$\sqrt{m}$]
$\Delta K_{II,corr}$	Cyclic corrected Mode II stress intensity factor [MPa$\sqrt{m}$]
$\Delta K_{III,corr}$	Cyclic corrected Mode III stress intensity factor [MPa$\sqrt{m}$]
$\mathrm{d}a/\mathrm{d}N$	Crack growth rate [mm/cycle]
μ	Poisson ratio [–]
ϕ	Crack kinking angle [°]
ϕ_0	Experimentally determined crack kinking angle [°]
ψ	Crack twisting angle [°]
$\psi_{0,III}$	Segment III twisting angle [°]
$\psi_{0,II}$	Segment II twisting angle [°]
$\psi_{0,I}$	Segment I twisting angle [°]
$\psi_{0,t/2}$	Central twisting angle [°]
ψ_0	Experimentally determined crack twisting angle [°]
σ	Pressure load [MPa]
σ_y	Yield strength [MPa]
ε_{el}	Elastic strain [–]
ε_{pl}	Plastic strain [–]
ε_{vm}	Von Mises strain [–]
A	Elongation at brake [%]
a	Crack length [mm]
a_i	Parameter for fitting function [–]
A_{pz}	Plastic zone area [mm^2]
a_x	Crack tip x-coordinate [mm]
a_y	Crack tip y-coordinate [mm]
a_z	Crack tip z-coordinate [mm]
b_i	Parameter for fitting function [–]
b_{pz}	Plastic zone width [mm]
c_i	Parameter for fitting function [–]
c_{pz}	Plastic zone circumferential length [mm]
d_i	Parameter for fitting function [–]
E	Young's modulus [GPa]
f	Test frequency [Hz]
F_{max}	Maximum test force [N]
h_{pz}	Plastic zone height [mm]
$K_{equ,\psi,corr}$	Corrected equivalent stress intensity factor [MPa$\sqrt{m}$]
$K_{equ,\psi}$	Angle-dependent Equivalent stress intensity factor [MPa$\sqrt{m}$]
K_{equ}	Equivalent stress intensity factor [MPa$\sqrt{m}$]
$K_{I,0}$	Mode I stress intensity factor for a straight crack [MPa$\sqrt{m}$]
$K_{I,\psi,corr}$	Corrected Mode I stress intensity factor [MPa$\sqrt{m}$]
$K_{I,\psi}$	Angle-dependent Mode I stress intensity factor[MPa$\sqrt{m}$]
$K_{II,\psi,corr}$	Corrected Mode II stress intensity factor [MPa$\sqrt{m}$]
$K_{II,\psi}$	Angle-dependent Mode II stress intensity factor [MPa$\sqrt{m}$]
$K_{III,\psi,corr}$	Corrected Mode III stress intensity factor [MPa$\sqrt{m}$]

$K_{III,\psi}$	Angle-dependent Mode III stress intensity factor [MPa$\sqrt{m}$]
K_{III}	Mode III stress intensity factor [MPa$\sqrt{m}$]
K_{II}	Mode II stress intensity factor [MPa$\sqrt{m}$]
K_{I}	Mode I stress intensity factor [MPa$\sqrt{m}$]
K_{max}	Maximum stress intensity factor [MPa$\sqrt{m}$]
m_t	Hardening modulus [MPa]
R	Load ratio [–]
r_{ppz}	Plastic zone radius [mm]
t	Specimen thickness [mm]
$t_{S,III}$	Segment III width [mm]
$t_{S,II}$	Segment II width [mm]
$t_{S,I}$	Segment I width [mm]
x	x-coordinate [mm]
y	y-coordinate [mm]
$Y_{eqv,\psi}$	Angle-dependent equivalent geometry factor [–]
$Y_{I,\psi}$	Angle-dependent Mode I geometry factor [–]
$Y_{II,\psi}$	Angle-dependent Mode II geometry factor [–]
$Y_{III,\psi}$	Angle-dependent Mode III geometry factor [–]
z	z-coordinate [mm]
APDL	Ansys parametric design language
CPZ	Cyclic plastic zone
DCPD	Direct current potential drop
DIC	Digital image correlation
FE	Finite element
HR-DIC	High resolution digital image correlation
L-T	Longitudinal-Transverse
M-T	Middle tension
PPZ	Primary plastic zone
PZ	Plastic zone
T-L	Transverse-Longitudinal

The CPZ is of particular importance as it reflects the fatigue damage inherent in the cyclic nature of the fatigue crack propagation process. Park et al. [5] and Chick et al. [6] demonstrated that the size of the CPZ can be correlated with the growth rates of fatigue cracks.

In order to study the PZ from a three-dimensional perspective, finite element (FE) simulations has been utilized to analyse the size and shape of both PPZ and CPZ. In particular, the numeric studies [7,8] revealed that the shape of the PPZ deviates from the classical dog bone model proposed by Dugdale [9] and depends significantly on the specimen thickness t and $K_{\max}$ [10]. For pure mode I loading, PPZ and CPZ are symmetrical to the crack path. However, this symmetry is lost when mixed-mode loading is present [11,12]. Using 3D finite element simulations, Zeinedini [13] shows that the shape of the PZ becomes asymmetric at a combination of mode I, II or III conditions. Furthermore, numerical investigations demonstrated that the T-stress, acting parallel to the crack, significantly influences the shape of the PPZ. Specifically, a positive or increasing T-stress compresses the PPZ, while a negative or decreasing T-stress elongates the PPZ in the crack propagation direction [14,15].

With the advent of digital image correlation (DIC) in experimental mechanics, there has been an increase in experimental investigations studying the PZ during fatigue crack growth. Prior to this, knowledge about the size and shape of the PZ was primarily derived from microhardness measurements, etching to assess dislocation density, optical interference, local strain gauge foils, or the identification of the recrystallization fraction at the crack tip [16]. The small dimensions of the PZ, which is only a few millimetres in size, require the use of high-resolution DIC systems [17]. Using an fixed optical light microscope, Besel et al. [10] investigated the shape of PZ at different specimen thicknesses and crack tip loads. However, due to the high resolution and, consequently, restricted measuring range, only a limited portion of the fatigue crack can be captured, thereby precluding an in-depth analysis of the entire fatigue crack at this level of detail. Consequently, Paysan et al. [18] proposed a novel robotic HR-DIC system that guides an optical light microscope and enables the automatic capture of the evolution of the PZ during the entire fatigue crack propagation process. Nevertheless, due to its small size, capturing the CPZ with HR-DIC remains a challenging task. For this reason, the majority of studies make the assumption that the CPZ undergoes changes that are comparable to those observed in the PPZ.

For simplicity, fatigue crack growth is often modelled in 2D, despite the fact that actual crack behaviour strongly depends on 3D effects. Therefore, current research focuses on investigating 3D effects such as different 3D crack shapes [19], stress states [20],

crack closure mechanisms [21], as well as thickness effects [22]. The crack front of a mode I fatigue crack can deviate from the flat geometry in 3D that is commonly assumed in 2D fracture mechanics. Especially, fatigue cracks in thin aluminium sheets tend to form shear crack front geometries as their crack tip stress increases [23–25]. Yamada et al. observed a transition from an initially flat fracture towards a double shear (*V-fracture*) or a single shear (*Slant fracture*) as well as transitions from double to single shear [26]. Such transitions can be associated with variations in growth rate [27]. Accompanying numerical studies attribute this phenomena to local decreases in the crack driving force, considering the mode I stress intensity factor as crack driving force [27,28]. This conclusion is supported by Esnault et al. [29], who performed different 3D FE simulations with crack front geometries extracted from fractured fatigue crack growth specimens. He also reported that the crack loading state changes from pure mode I loading to mixed-mode loading along the crack front. Current research suspects that these shape changes of the crack front are due to local interactions between the stress state and the material's microstructure [30]. However, the actual local mechanisms are still not fully understood.

Due to its high damage tolerance behaviour, the aluminium alloy AA2024-T3 is widely used in fuselage structures [31]. The rolling process of the sheet material production leads to anisotropy, resulting in different mechanical behaviours perpendicular and parallel to the rolling direction.

Bergner et al. [32] studied the fatigue crack growth behaviour in multiple different rolled aluminium alloys. He showed that within the Paris regime, T-L fatigue cracks tend to propagate faster than L-T cracks. Antunes et al. [33] agreed with these observations regarding the different growth rates in the L-T and T-L directions, attributing the differences to different crack closure behaviour. Jian et al. [34] hypothesize a relationship with the spacing of grain boundaries. They examined CT specimens with different grain sizes and observe that smaller grain sizes result in slower crack growth rates. They concluded that both the grain boundaries and the precipitates at the grain boundaries of aluminium alloys act as barriers to fatigue crack growth, and thereby delaying it. Wei et al. [35] and Esin et al. [36] support these observations regarding the different crack propagation behaviours in the L-T and T-L directions. They correlate this with the increased occurrence of crack deflections and bifurcations as a result of frequent local changes in crystallographic orientation in the L-T direction. Zheng et al. [37] also reaches this conclusion in their studies of AA2524-T34.

This paper investigates the relationship between the twist of the crack front, its impact on the PZ at the crack tip as well as the crack tip loadings, and the evolution of the crack propagation curve $\mathrm{d}a/\mathrm{d}N - \Delta K$. To achieve this, crack propagation experiments are performed on MT160 specimens of AA2024-T3 in both L-T and T-L crack orientations. These experiments are conducted in parallel with a HR-DIC robotic system, which provides detailed displacement field data near the crack tip during entire fatigue crack growth. The implemented algorithms identify the PPZ within the HR-DIC data and characterize its shape and size, aiming to correlate these parameters with the local geometry of the fatigue crack front. Therefore, the fracture surfaces were digitalised with a 3D scanner after the tests in order to supplement the data set. Finite element simulations are utilized to derive a mapping function that adjusts ΔK to ΔK_{eqv}, accounting for the mixed-mode loading conditions induced by the twisted crack front. Finally, we investigated whether the twisted crack front geometries observed in L-T and T-L fatigue cracks contribute to the variations in propagation rates and consequently to the $\mathrm{d}a/\mathrm{d}N - \Delta K$ curves.

2. Methods

2.1. Material characterization

The study investigates fatigue crack growth in a rolled aluminium AA2024-T3 (AlCu4Mg1) sheet material with a thickness of 2 mm. The mechanical properties along the rolling direction are provided by the commercial supplier: Yield strength $\sigma_{\mathrm{yield}} = 345$ MPa, ultimate tensile strength $R_{\mathrm{m}} = 466$ MPa, elongation at brake $A = 18\%$. As stated in [38], the material displays a rolling direction-dependent anisotropy.

2.2. Experimental setup

The investigated specimens are standardized middle tension (MT 160) specimen (Width = 160 mm) in T-L and L-T orientation. The crack propagation tests were performed in accordance to the ASTM E674-13 standard [1] at a load ratio of $R = 0.1$ and a maximum load of $F_{\mathrm{max}} = 15$ kN. Fatigue crack growth starts from an artificial notch with a length of $2a = 16$ mm located in the centre of the specimen. The fatigue crack propagation tests were then carried out with a sinusoidal load and a constant amplitude at a test frequency of $f = 20$ Hz. The crack length was measured with the direct current potential drop (DCPD) method at two pins 10 mm above and below the initial saw notch [39]. DIC was employed for full-field displacement measurements on both sample surfaces. A commercial GOM ARAMIS 12 m 3D DIC system captures the surface deformations at the backside of the specimen. With a facet size of 25 x 25 pixels and a facet spacing of 16 pixels, the system allows for a spatial resolution of 0.72 mm per facet. At the front side, a KUKA LBR iiwa cobot moves a Zeiss STEMI 206C stereo microscope with a Basler a2A5320-23umPRO global shutter CMOS camera (Fig. 1(a)). This HR-DIC system captures 2D displacement fields (Fig. 1(c)) with a field of view is 10.2 mm x 5.7 mm near the crack tip position. For DIC evaluation, a refined iron oxide speckled airbrush pattern is applied at the specimen front side. Using a facet size of 40 x 40 pixels and a facet distance of 30 pixels, a spatial resolution of 0.047 mm per facet was achieved. Further details of the test stand can be found in [18]. This multi-scale DIC setup allows sufficient resolution to analyse the PPZ of the propagating crack, but also to determine the deformation of the entire sample. During the test, images were taken after crack propagation increments of $\Delta a = 0.5$ mm for minimum, intermediate and maximum load. The displacement and strain fields were calculated by the GOM ARAMIS V2020 software. In order to retrieve the total strain or displacement fields, the images taken at each load step were correlated to a reference image taken at zero load before fatigue crack growth experiment started. After the test, the crack propagation curve $\mathrm{d}a/\mathrm{d}N - \Delta K$ was determined in accordance to ASTM E674-13 [1].

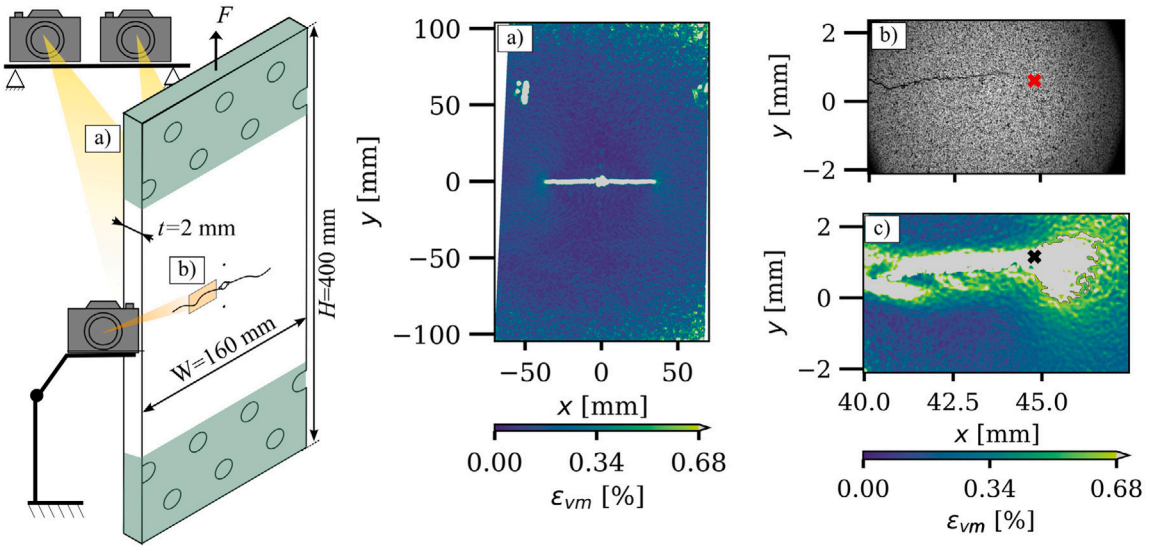

Fig. 1. Overview of experimental setup and numerical model: MT-160 specimen with 2D HR-DIC and 3D DIC system, (a) strain field captured by 3D DIC, (b) High resolution microscope image of crack growth, with detected crack tip, (c) strain field captured by 2D HR-DIC.

2.3. Plastic zone evaluation

Feature extraction and dimension reduction is performed to quantify the contour of the PZ using descriptors. In this way, the contour can be described using variables and can be related to other variables obtained from the fracture surface analysis and the crack propagation tests. To facilitate direct comparison, features of the contour of the PZ were quantified using both HR-DIC displacement and nodal data of the free surface of the 3D finite element model. The contour identification of the PZ always refer to the strain field at maximum load. Within the frame of this paper, we consider as PZ all plastic deformations in front of the crack tip. That means, that the PZ identified includes both the PPZ and CPZ.

Fig. 2(a) illustrates features that characterize the PZ based on the surface nodal data of the 3D FE model. The procedure is applied in Fig. 2(b) to the experimental 2D HR-DIC fatigue crack growth data and is described in more detail below. While in the FE data the crack tip location is known, we need to detect it within the HR-DIC data. This is achieved automatically by employing a machine learning model proposed by Melching et al. [40] and Strohmann et al. [41]. In order to distinguish between elastic–plastic and linear-elastic deformations, we used HR-DIC data at maximum load as the strain field is less affected by inherent scatter. Within the captured DIC strain field, one cannot separate directly between elastic and plastic deformation, therefore we need a simplification. To identify the PZ region, we defined a threshold of 0.68% related to the von Mises equivalent strain $\varepsilon_{\mathrm{vm}}$. The value of $\varepsilon_{\mathrm{vm}} = 0.68\%$ represents a uni-axial estimation of the yield criterion, as defined by a simplified approach:

$$\varepsilon_{\mathrm{total}} = \varepsilon_{\mathrm{el}} + \varepsilon_{\mathrm{pl}} = \frac{R_{\mathrm{p0,2}}}{E} + \varepsilon_{\mathrm{pl}} \tag{2}$$

with $\varepsilon_{\mathrm{pl}} = 0.2$ according to the definition of $R_{\mathrm{p0,2}}$. Furthermore, all elastic–plastic deformations behind the detected crack tip are neglected. Due to sensitivity of the optical sensors, air movement, varying lighting conditions, reflections, the speckle pattern quality or out-of-plane motion, DIC images are subjected to inherent noise that affect the DIC evaluation [42–44]. This causes that several contours despite to the actual PZ might be identified. In such instances, these are regarded as artefacts and are excluded from subsequent analysis. As the FE results are not affected by scattering, the plastic zone is consistently delineated by a smooth contour. The area of PZ contour A_{pz} encloses the masked area (see black contours in Fig. 2(a) and (b)). The ratio between upper wing A_1 and lower wing A_2, being separated by a line between crack tip and minimum contour extension, describes the area difference ΔA_{pz}. The height h_{pz} is defined as horizontal distance between minimum and maximum horizontal extension point. In comparison, the length b_{pz} denotes vertical distance between minimum and maximum vertical extension point (Fig. 2).

2.4. Fracture surface characterization

After fatigue crack propagation testing, the fractured specimens were scanned with a GOM ATOS Q 12M 3D scanner in order to obtain their topography of the fracture surfaces in a digital format. The coordinate origin of the z-axis is set to the centre of the specimen and aligned with the coordinate system of the DIC system. In the next step, we aim to assign the local fracture surface shape to a certain fracture type. In total, four different fracture types are distinguished: flat, transition, S-fracture, and V-fracture. Fig. 5 shows an overview of the fracture types classified in this paper, while Fig. 3 clarifies the understanding of the crack kink angle ϕ_0 (a) and the crack tilt angle ψ_0 (b). To determine ψ_0, cutting planes in depth direction (y–z plane) are set along the x-axis with a

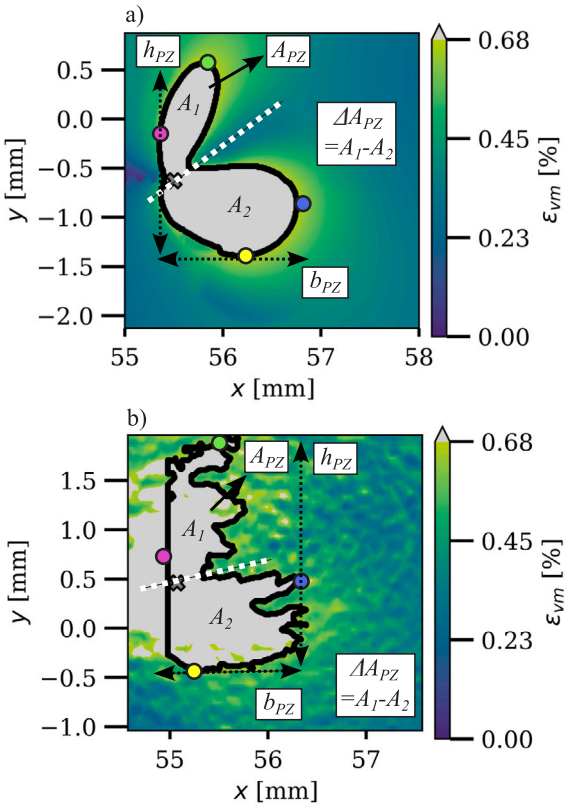

Fig. 2. (a) Numerically determined plastic zone at the surface strain field with dimension points and definitions of height h_{pz}, length b_{pz} and division line between upper area A_1 and lower area A_2, (b) experimentally determined plastic zone in HR-DIC data with same; Example here: T-L, $a_x = 55.1$ mm, $a_y = 0.37$ mm, $\Delta K_{\mathrm{I,ASTM}} = 25.1$ MPa$\sqrt{\mathrm{m}}$, $\Delta K_{\mathrm{I,corr}} = 21.8$ MPa$\sqrt{\mathrm{m}}$, $\Delta K_{\mathrm{II,corr}} = -0.009$ MPa$\sqrt{\mathrm{m}}$, $\Delta K_{\mathrm{III,corr}} = -13.2$ MPa$\sqrt{\mathrm{m}}$, $\psi_0 = -31.10°$, $\phi_0 = -0.9°$.

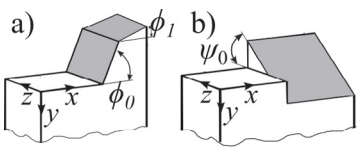

Fig. 3. Definition of (a) kink angle ϕ_0 and (b) tilt angle ψ_0.
Source: Adapted from [45].

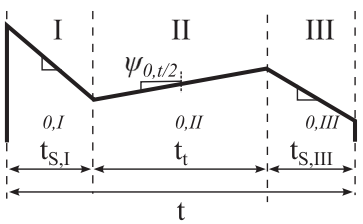

Fig. 4. Angle and segment definition for shear lip and fracture mode evaluation.

spacing of 0.1 mm. Thus, the local fracture surface contour is given by single data points in 2D. To include only the fractured surface and disregard data points from scanning singularities, the left and the right 10% of the projected surface contour of the y-z plane are neglected (Fig. 6, grey marked area). The remaining contour is approximated piece by piece linearly with in three segments [47]. The length and slope of the single three segments are variable and set by the algorithm. To assess the quality of the fitted lines, we determine a correlation coefficient comparing the linear curve segment approximation and the original contour points. Furthermore, the tilt angle difference of the central segment $\psi_{0,t/2}$ towards the outer segments $\psi_{0,I,III}$, the lengths of the outer segments $t_{S,I,III}$

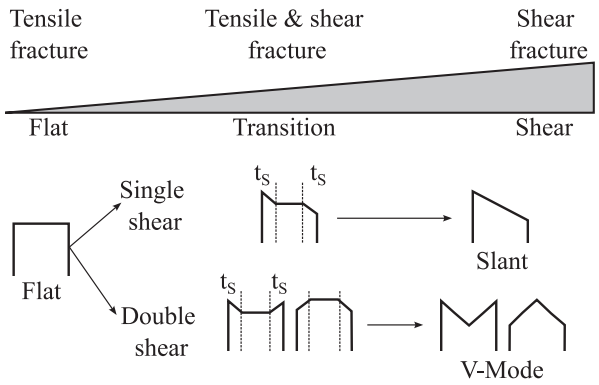

Fig. 5. Visualization of classified fracture types with transition from flat to shear fracture according to [46].

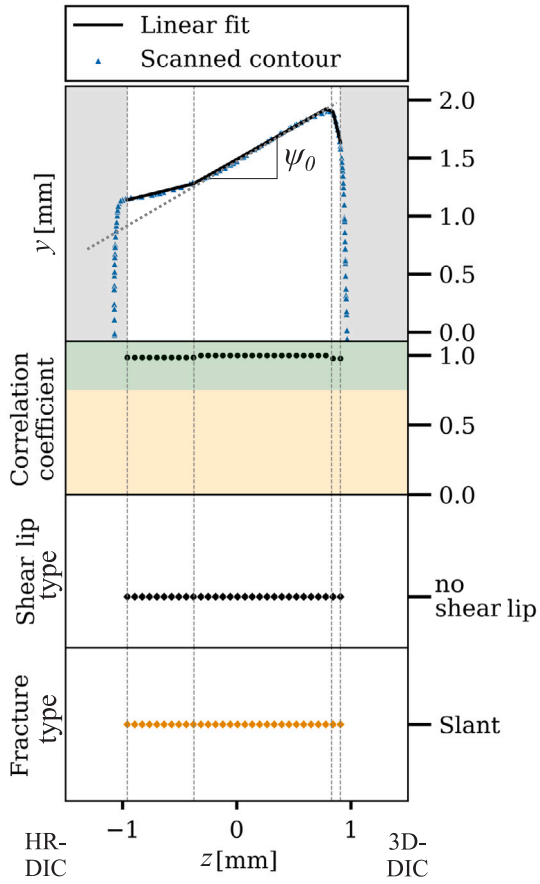

Fig. 6. Example of evaluation of slant fracture types of L-T specimen at crack length $a_x = 52$ mm.

and the linear fit correlation coefficient are taken into account for determining the fracture type. Fig. 4 outlines the angle and segment definition. Significant slope differences between the outer segments and the centre one are associated with shear lips [48].

The following conditions have to be met to classify shear lips:

- Segment correlation coefficient > 0.75
- Segment position index $j = I, III$
- Segment angle difference towards central angle $|\psi_{0,j} - \psi_{0,t/2}| > 15°$

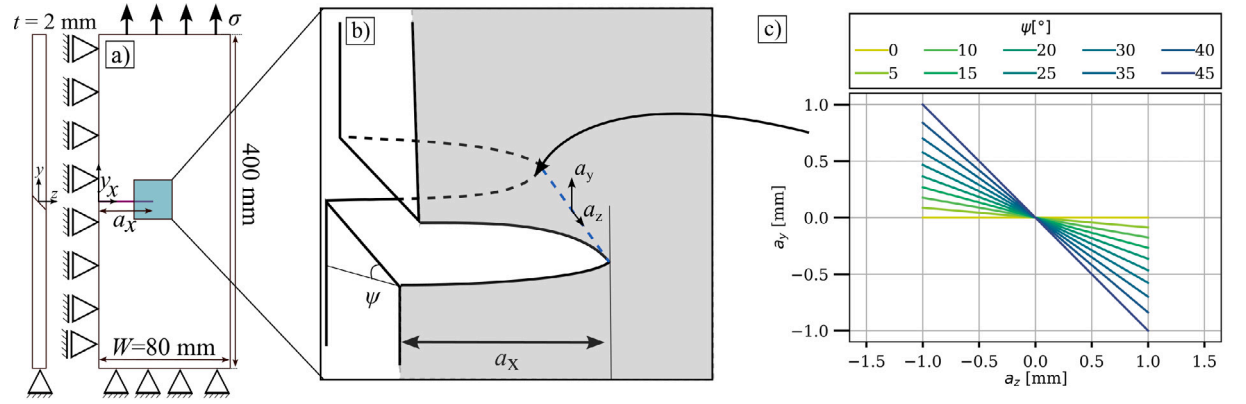

Fig. 7. (a) Numerical 3D model with boundary conditions, (b) Detail view of modelled crack front depending on crack front position and tilt angle, (c) Visualization of crack front depending on tilt angle ψ.

- $0.05 < t_{S,j}/t < 0.4$

The criteria for fracture more characterization are given by:

- S-fracture type: $|\psi_{0,t/2}| > 5°$ and $t_t/t < 0.5$
- Flat fracture type: $|\psi_{0,t/2}| < 5°$ and $t_t/t < 0.5$
- V-fracture type: $|\psi_{0,t/2}| < 5°$ and $t_t/t > 0.3$
- Transition: $|\psi_{0,t/2}| > 5°$ and $t_t/t > 0.5$

2.5. Numerical analysis

In order to analyse the relation between PZ and crack front twisting, we perform multiple elastic–plastic 3D FE simulations with different crack front twisting angles ψ_0 and crack lengths a/W. Furthermore, linear elastic simulations were performed to outline the dependence of tilt angle ψ_0 on the stress intensity factors $K_{\mathrm{I}}, K_{\mathrm{II}}, K_{\mathrm{III}}$ along the crack front. The simulations were performed with ANSYS Mechanical APDL Version 2022 R1 on a RedHat Linux Workstation with two Intel Xeon Gold 6240 18C CPUs and a total DDR4-2933 RAM of 256 GB . Material properties of the AA2024-T3 aluminium alloy are taken according to the literature [49]. Young's modulus and Poisson ratio were set to $E = 73.1$ GPa and $\mu = 0.33$. Hardening modulus and yield stress were set to $m_t = 984$ MPa and $R_{p,0.2} = 345$ MPa, using a bilinear isotropic hardening model (APDL: BISO) for elastic–plastic simulations.

The MT160 model was meshed using free mesh and tetrahedral SOLID187 elements with quadratic displacement behaviour. To reduce the complexity of the model, we use its symmetrical property to half the model $W/2 = 80$ mm (APDL: D, ALL, UX, 0). According to the experimental setup, the lower surface was clamped in all directions (APDL: D, ALL, ALL, 0) and a constant load was applied at the top surface (APDL: SFA, ALL, PRES, σ) with a set of coupled nodal displacements (see Fig. 7). This represents the clamped upper side of the test setup (Fig. 1, green area). The overall mesh is subdivided in a global mesh with an element size of 1 mm and a refined area around the crack tip (APDL: NREFINE) with an element size of 0.042 mm for the linear-elastic simulation. For the elastic–plastic simulation, the domain of mesh refinement was set by estimating the PZ size according to Irwin's formula (Eq. (1), under plane stress conditions) for $a_x/W = 0.8$ and a $K_{\mathrm{I}} = 50$ MPa$\sqrt{\mathrm{m}}$, leading to a refinement area of $r_{\mathrm{p}} = 3.2$ mm starting from the crack tip. This leads to a refined element size of 0.037 mm and a model with a total of 1.079.885 nodes.

Table 1 enumerates the parameters for evaluating the dependency of the crack front tilt angle ψ on PZ surface geometry and the crack tip stress along the crack front. The stress intensity factors $K_{\mathrm{I,II,III}}$ are calculated for each node of the crack front by using the volume interaction integral provided in ANSYS (APDL: CINT). This method returns a mean value of six integration paths for each node along the crack front. The node-individual stress intensity factors are then averaged over the crack front. In order to facilitate a comparison between the experimentally determined PZ and the numerical model, the parameters presented in Fig. 8 were utilized in an additional study which acts as a digital twin for the experiment. Therefore, the experimentally determined crack path coordinates a_x and a_y and the tilt angle ψ_0 of the fracture surfaces are applied to the FE model. A total number of 36 simulations were carried out for the L-T specimen and 29 simulations for the T-L specimen.

3. Results

3.1. Crack propagation curve $\mathrm{d}a/\mathrm{d}N - \Delta K_{\mathrm{I}}$

Fig. 9 compares the crack propagation curves $\mathrm{d}a/\mathrm{d}N$ vs. ΔK_{I} for both tested crack orientations L-T and T-L evaluated according to ASTM E674-13. Three distinct sections can be identified:

Table 1
Parameter for elastic–plastic parameter study of the influence of tilt angle towards shape of plastic zone.

Parameter	Variations
Length to width ratio a/W	a/W = [0.3, 0.4, 0.5, 0.6, 0.7, 0.8]
Crack tip a_x	a_x = [16, 24, 32, 40, 48, 56, 64] mm
Tilt angle ψ	ψ = [0, 5, 10, 15, 20, 25, 30, 35, 40, 45]°

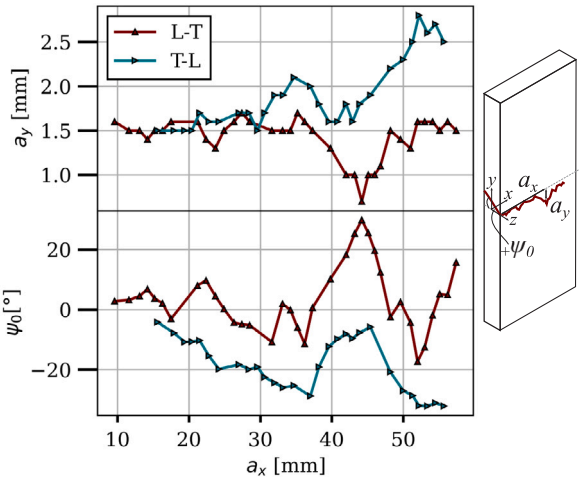

Fig. 8. Experimentally determined input parameter crack path a_x, a_y and tilt angle ψ_0 for elastic–plastic simulation of the plastic zone of L-T and T-L specimen.

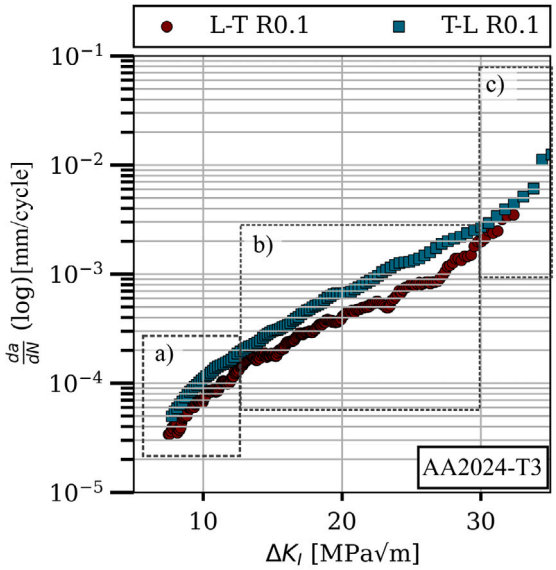

Fig. 9. Comparison of crack propagation curve $\mathrm{d}a/\mathrm{d}N - \Delta K_\mathrm{I}$ of L-T and T-L oriented specimen with categorization in three sub-areas.

- In section (a), the crack propagation behaviour of L-T and T-L orientations is approximately comparable in terms of propagation rate and stress intensity factor. However, the L-T crack propagates slightly faster than the T-L crack.
- Section (b) begins at $\Delta K_\mathrm{I} > 13\ \mathrm{MPa}\sqrt{\mathrm{m}}$ and a crack propagation rate of $\mathrm{d}a/\mathrm{d}N > 2 \cdot 10^{-4}$ mm/cycle. From this point, the propagation rate of the T-L fatigue crack increases faster than the T-L one leading to significant distances between both crack propagation curves. Additionally, the crack propagation curve of the L-T specimen exhibits fluctuations in the crack propagation rate, while the T-L curve is relative smooth.
- For $\Delta K_\mathrm{I} > 30\ \mathrm{MPa}\sqrt{\mathrm{m}}$ and $\mathrm{d}a/d\mathrm{N} > 2 \cdot 10^{-4}$ mm/cycle, section (c) begins. Here, both curve progress similar towards a common crack propagation rate.

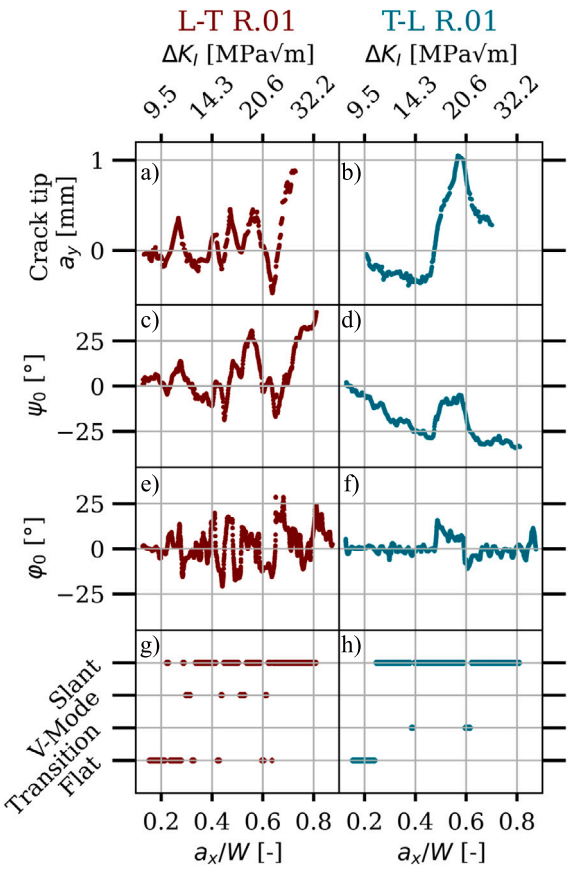

Fig. 10. Comparison of the experimentally determined parameters from HR-DIC evaluation and fracture surface characterization, (a,b) microscopical crack path, (c,d) tilt angle ψ_0, (e,f) kink angle ϕ_0, (g,h) classified fracture types.

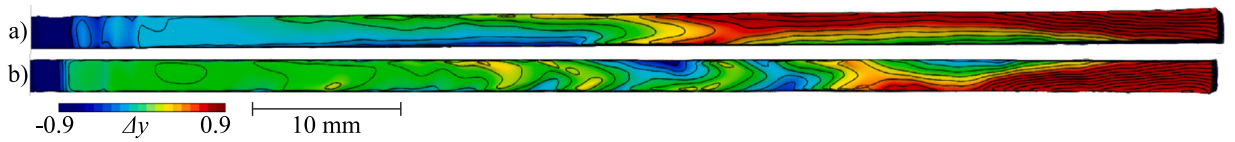

Fig. 11. Top view and comparison of the fracture surface captured via 3D Scan with height difference Δy towards initial crack plane, (a) T-L specimen, (b) L-T specimen.

3.2. Characterization of the three-dimensional crack propagation behaviour based on fracture surface analysis

Fig. 11 visualizes the topography of the fracture surfaces of T-L and L-T specimen captured via 3D scan. Using the line segmentation method described in 2.4, to assign the four different fracture types locally along the crack path. Fig. 10 compares the crack path from HR-DIC evaluation (a,b), tilt angle ψ_0 (c,d), kink angle ϕ_0 (e,f) as well as the classified fracture types (g,h). The stress intensity factor ΔK_I was calculated according to [1] with regards to the specimen geometry for the experimentally given parameters load ratio $R = 0.1$, maximum load $F_\mathrm{max} = 15$ kN and the crack length a evaluated via DCPD. As the size of the PZ exceeds the microscopic field of view or measurement rage, data points in Fig. 10(a) and (b) are missing for $\Delta K_\mathrm{I} > 25\mathrm{MPa}\sqrt{\mathrm{m}}$ and $a_x/W > 0.7$, respectively. Regarding the crack path, the L-T orientated specimen shows an irregular crack path with several turning points in a stress intensity factor range between 11 and 25 $\mathrm{MPa}\sqrt{\mathrm{m}}$. This behaviour is also evident in the fracture pattern, where periodic crack kink and tilt can be observed. This turn results in multiple tilting of the crack front leading to multiple changes in the fracture types up to a range of 25 $\mathrm{MPa}\sqrt{\mathrm{m}}$. Regarding the T-L orientated specimen, the crack path remains fairly stable and straight. The crack path changes its direction only twice at 16 $\mathrm{MPa}\sqrt{\mathrm{m}}$ and 19 $\mathrm{MPa}\sqrt{\mathrm{m}}$ which is accompanied with crack kinking and a change in the tilt direction. This leads to crack fronts with less changes in fracture types compared to L-T. The direction of a

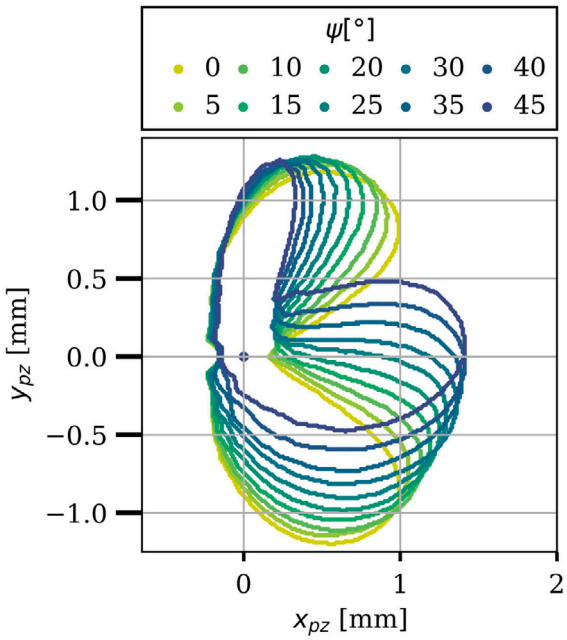

Fig. 12. Contour of the plastic zone at $K_I = 29.9$ MPa$\sqrt{m}$ with different crack front tilt angle ψ.

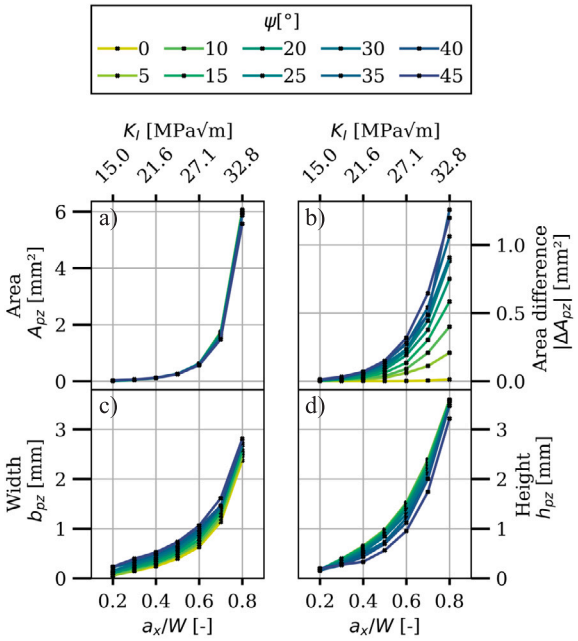

Fig. 13. Numerical results of the plastic zone: (a) area A_{pz} and estimation according to (1), (b) absolute wing area difference ΔA_{pz}, (c) width b_{pz}, (d) height h_{pz}.

crack path may undergo a change when the tilt angle, ψ_0, undergoes a reversal. This can result in a change in fracture type, as the tilt angle is a criterion for identifying a slant fracture.

3.3. Parameter study: Influence of tilt angle and load on the shape and size of the plastic zone

Fig. 12 compares the contour of simulated PZ at the specimen surface for a nominal $K_I = 30$ MPa$\sqrt{m}$ and a variation ψ_0. It illustrates that with increasing tilt angle ψ_0 the contour evolves more and more asymmetric. The shape also differs from the classical and symmetric dog-bone model [9]. It is also evident that the area of the lower wing increases as the tilt angle increases, while

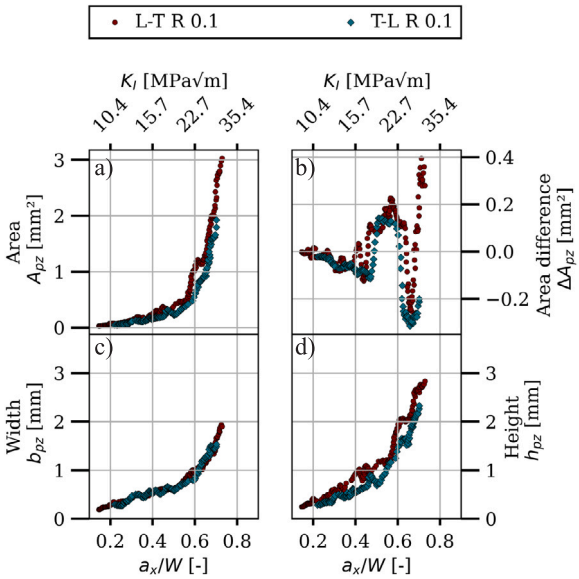

Fig. 14. Characterization of the experimentally determined plastic zone: (a) area A_{pz} and estimation according to (1), (b) absolute wing area difference ΔA_{pz}, (c) width b_{pz}, (d) height h_{pz}.

the area of the upper wing decreases. As introduced in Section 2.3, Fig. 13 illustrates the dependency of the geometry parameters, namely (a) area A_{pz}, (b) wing area difference $|\Delta A_{pz}|$, (c) width b_{pz} and (d) height h_{pz} at different crack lengths or stress intensity factors, respectively. The area A_{pz} shows a quadratic relationship along the stress intensity factor K_I that reflects the power law proposed by Irwin and given in formula (1) [50]:

The comparison of the elastic–plastic simulation to the estimation based on formula (1) emphasis that Irwins size estimation underestimates the area of the PZ, which is also stated by Jia [51]. It is interesting that the area A_{pz} seems to be independent from the tilt angle ψ_0. This is explained that the energy input each cycle is constant and does not depend on the tilted crack front. Also Li et al. reported angle-independent plastic energy dissipation within the PZ [52]. Width b_{pz} and height h_{pz} also show a quadratic relationship to K_I, but also a dependency from tilt angle ψ_0. When the tilt angle increases, the shape of the PZ tilts along the x-axis. This leads to a reduction in height around 10% for each increasing angle increment. The lower wing expands, leading to an increased width b_{pz}. Both characteristics depend on K_I and the tilt angle ψ_0. This is also evident from the absolute area difference between the upper and lower wing $|\Delta A_{pz}|$, which emphasis the significant asymmetry of the shape. An increasing tilt angle ψ_0 leads to an increased width b_{pz} which results in an asymmetric area ratio $|\Delta A_{pz}|$ of the upper and lower wing.

3.4. Characterization of the experimentally determined plastic zone

Fig. 14 compares the (a) area A_{pz}, (b) the wing area difference ΔA_{pz}, (c) width b_{pz} and (d) the height h_{pz} for the experimentally determined plastic zones of the L-T and T-L oriented specimens. As also stated in Section 3.3 for the numerical analysis, the experimentally determined area A_{pz}, width b_{pz} and height h_{pz} also show a quadratic relationship to K_I. While the width b_{pz} does not show a dependency of the orientation, the plastic zone area A_{pz} and height h_{pz} differs for L-T and T-L orientation. At the same stress intensity factor K_I, the area of the PZ of the L-T oriented specimen is up to 30% greater and the height differs up to 35%. As seen in Fig. 14(a), the area increase up to a $K_I = 20\ \mathrm{MPa}\sqrt{\mathrm{m}}$ for L-T and $K_I = 25\ \mathrm{MPa}\sqrt{\mathrm{m}}$ for T-L is comparable with the estimation according to Irwin. The qualitative progression of the curve corresponds more closely to the simulation results given in Fig. 13. The analysis of the wing area difference ΔA_{pz} in Fig. 14(b) outlines an exponential increase for increasing K_I for both orientations. The curve for L-T shows more fluctuations around the zero line, where both wings are the same size. The increase in ΔA_{pz} indicates increasing asymmetry, while the change in sign indicates a change in the size ratios of the wings.

3.5. Parameter study: Influence of tilt angle on stress intensity factors K_I, K_{II}, K_{III}, K_{eqv}

Fig. 15 outlines the dependency of the tilt angle ψ and normalized crack length a_x/W on the geometry factors $Y_{I,\psi}, Y_{II\psi}, Y_{III\psi}, Y_{eqv\psi}$. In order to calculate the equivalent stress intensity factor K_{eqv}, Richard's formula [45] is used.

$$K_{eqv} = \frac{K_I}{2} + \frac{1}{2}\sqrt{K_I^2 + 4 \cdot K_{II}^2 + 5.336 \cdot K_{III}^2} \tag{3}$$

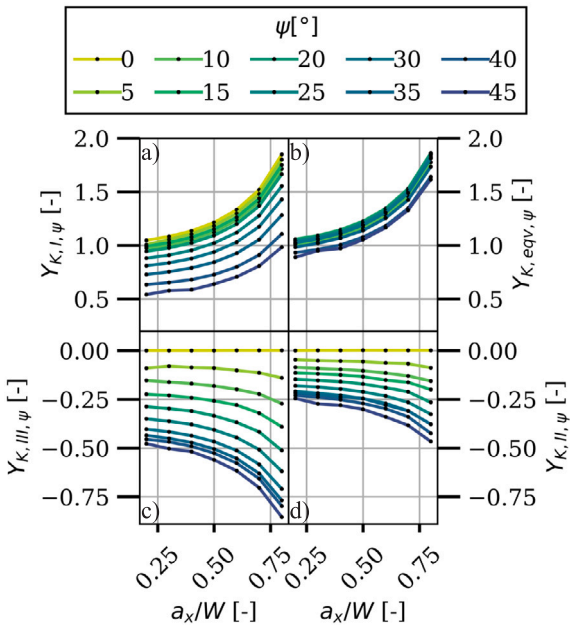

Fig. 15. Geometry factors (a) mode I Y_{I}, (b) equivalent stress intensity factor Y_{eqv}, (c) mode III Y_{III}, (d) mode II Y_{II}, depending on tilt angle ψ.

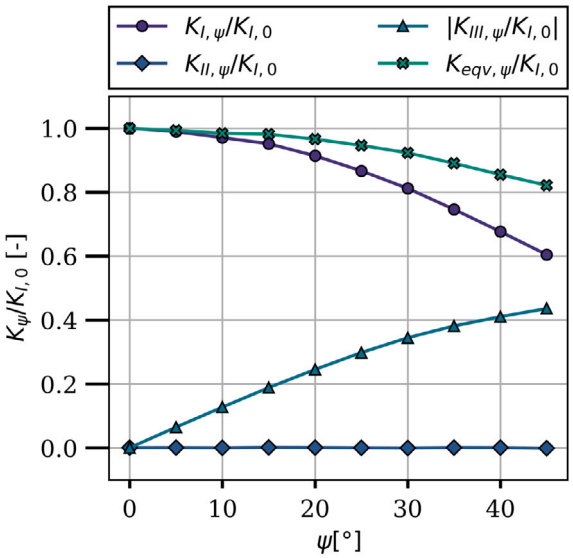

Fig. 16. Normalized stress intensity factors $K_{i,\psi}$.

The geometry factors corresponding to the nominal load are normalized using the equation

$$K_{i,\psi} = \frac{F}{W \cdot t} \cdot \sqrt{\pi \cdot a} \cdot Y_{i,\psi} \tag{4}$$

where $i = [\mathrm{I}, \mathrm{II}, \mathrm{III}, \mathrm{eqv}]$.

As the tilt angle ψ increases, $Y_{\mathrm{I},\psi}$ decreases up to 40%. Crack tilting also leads to a mixed-mode-loading condition as evidenced in the increase of $Y_{\mathrm{II},\psi}$ and $Y_{\mathrm{III},\psi}$, where $Y_{\mathrm{III},\psi}$ is pre-dominant compared to $Y_{\mathrm{II},\psi}$. Fig. 15 shows that crack tilting also impacts the mixed-mode equivalent stress intensity factor $Y_{\mathrm{eqv},\psi}$, which decreases by 20% compared to the decrease in $Y_{\mathrm{I},\psi}$.

Fig. 16 shows the stress intensity factors $K_{i,\psi}$ normalized towards the stress intensity factor of a straight crack $K_{\mathrm{I},0}$ as a function of ψ. Using this relationship, we derive a mapping function to describe the mixed-mode loading distribution of $K_{i,\psi,corr}$ when the

Table 2
Parameters for fitting function to calculate $K_{i,\psi}$ based on a given tilt angle ψ and stress intensity factor for a straight crack $K_{I,0}$.

SIF	$a_i \cdot 10^{-4}$	$b_i \cdot 10^{-4}$	$c_i \cdot 10^{-4}$
$K_{I,\psi,corr}$	−1.77	−9.14	10 000
$K_{II,\psi,corr}$	−0.015	0.445	4.42
$K_{III,\psi,corr}$	−1.08	147	−47.7
$K_{eqv,\psi,corr}$	−0.928	2.51	9966

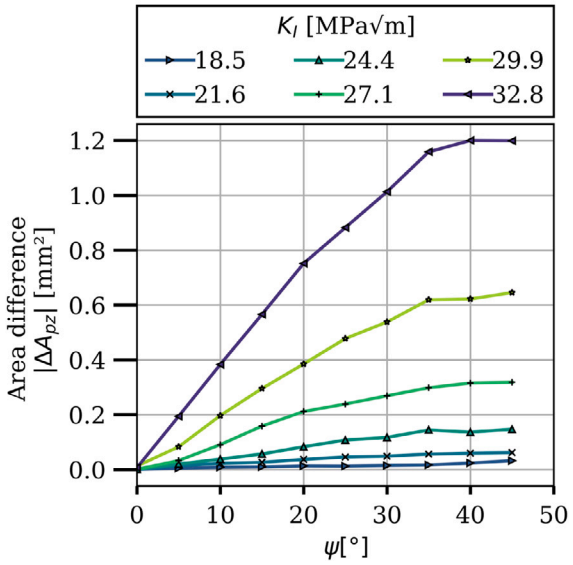

Fig. 17. Relationship between crack front tilt angle ψ and area difference of the plastic zone wings $|\Delta A_{pz}|$ at different K_I based on the numerical studies.

Table 3
Experimentally determined tilt angle ψ_0, kink angle ϕ_0, Area difference $|\Delta A_{pz}|$ and stress intensity factors $\Delta K_{i,\psi,corr}$ for plastic zone contours pictured in Fig. 18.

No.	Orientation	ψ_0 [°]	ϕ_0 [°]	$\lvert\Delta A_{pz}\rvert$ [mm²]	$\Delta K_{I,\psi,corr}$ [MPa $\sqrt{m}$]	$\Delta K_{III,\psi,corr}$ [MPa $\sqrt{m}$]
(a)	L-T R0.1	−9.78	4.4	–	14.1	−1.0
(b)	L-T R0.1	1.9	−11.5	0.08	20.2	0.6
(c)	T-L R0.1	−24	0	–	15.3	−6.5
(d)	T-L R0.1	−27.0	−4.2	0.33	19.3	−11.6

crack tilt angle ψ and the stress intensity factor for a straight crack $K_{I,0}$ are known. By utilizing a quadratic fitting approach, $K_{i,\psi,corr}$ can be calculated as follows:

$$K_{i,\psi,corr} = (a_i \cdot \psi^2 + b_i \cdot \psi + c_i) \cdot K_{I,0} \tag{5}$$

This equations allows the estimation of K_{eqv}, although only $K_{I,0}$ is known and the local tilt angle ψ_0. The parameters needed for the equation above are given in Table 2.

4. Discussion

4.1. Relationship between experimentally crack tilt angle ψ_0 and plastic zone shape difference ΔA_{pz}

Fig. 17 outlines the relationship between the wing area difference $|\Delta A_{pz}|$ and tilt angle ψ. $|\Delta A_{pz}|$ increases linearly both with increasing tilt angle ψ and with increasing K_I. This implies that the crack front angle behaves approximately proportionally to the area difference. Therefore, by comparing the wing areas of the PZ on the surface of a mode I fatigue crack, it is possible to perform an in-situ assessment of the 3D crack front tilt angle. Consequently, the 2D characteristics observed at the surface allow for an 3D evaluation within the volume.

In order to validate the numerical derived proportional relationship between ΔA_{pz} and ψ_0, Fig. 18 compares an example of the experimentally and numerically determined PZ at K_I for both L-T (a,b) and T-L (c,d) orientation according to Table 3. For a better

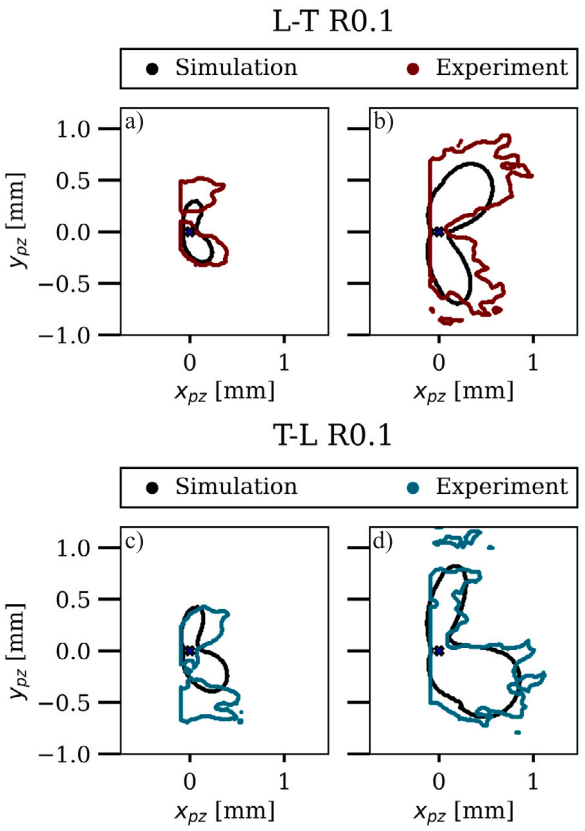

Fig. 18. Comparison of experimentally and numerically determined plastic zones according to parameters given in Fig. 8.

comparison, the coordinates x_{pz}, y_{pz} are normalized towards the crack tip position. In terms of overall size and shape, there is good agreement between experimental and numerical results proving that the PZ shapes of the experimental fatigue cracks results from the tilted crack front. At higher K_{I} the asymmetry and thus the wing area difference $|\Delta A_{\mathrm{pz}}|$ within the shape increases, as analysed in Fig. 17.

The comparison between experimental and numerical analyses in Fig. 19 also highlights the proportional dependence of the asymmetry of the PZ ΔA_{pz} to the crack front tilt angle ψ_0 as also outlined in Fig. 17 from a numerical perspective. Here, ψ_0 follows ΔA_{pz} nearly perfectly and confirms the relationship between both descriptors that have been outlined in Fig. 17. Previously, the symmetry loss of the PZ in the presence of a mixed mode loading state has been primarily studied numerically [12,13]. Our numerical and experimental results demonstrate that the tilted crack front creates a local mixed-mode loading state that leads to a significant asymmetry of the PZ. Furthermore, the authors of this paper add that using $|\Delta A_{\mathrm{pz}}|$ behaves approximately linear to the tilted crack front angle ψ_0 and, thus, allows for an in-situ estimation of the 3D tilted crack front. We conclude, that surface-based, 2D information based on the crack tip strain field can represent 3D crack front geometries. In standardized fatigue crack growth experiments, the fracture modes and three-dimensional features are usually neglected, and the understanding of their effects towards crack propagation behaviour is limited [53]. By numerically identifying and experimentally confirming the relationship between three- and two-dimensional crack-describing quantities, a better understanding of three-dimensional effects regarding crack propagation behaviour can be obtained.

4.2. Effect of tilting on stress intensity factors

In this section, the authors want to clarify if the different tilted crack fronts in L-T and T-L can explain their different crack propagation curves $\mathrm{d}a/\mathrm{d}N - \Delta K_{\mathrm{I}}$, shown in Fig. 9. By using the stress intensity factor ΔK_{I} and the experimentally determined crack tilt angle ψ_0 as inputs, we apply the derived mapping function in Eq. (5) to adjust ΔK_{I} to ΔK_{eqv}. Fig. 20 illustrates shows the adjusted $\mathrm{d}a/\mathrm{d}N - \Delta K_{\mathrm{eqv}}$. ΔK_{eqv} considers the mixed-mode loading state caused by the tilted crack front, while the crack propagation curve based on ASTM E647-15 in Fig. 9 only assumes a pure mode I loading. Fig. 20 illustrates that, particularly between 10 MPa$\sqrt{\mathrm{m}}$ and 28 MPa$\sqrt{\mathrm{m}}$ (section (b) in Fig. 9), both curves, L-T and T-L, exhibit a high degree of superposition. It indicates that the different tilted crack front geometries in L-T and T-L might be a reason for their crack propagation discrepancies. Next to the barrier impact of grain boundaries and participates, that we support the statement of Weil et al. [35] and Esin et al. [36] that geometrical differences

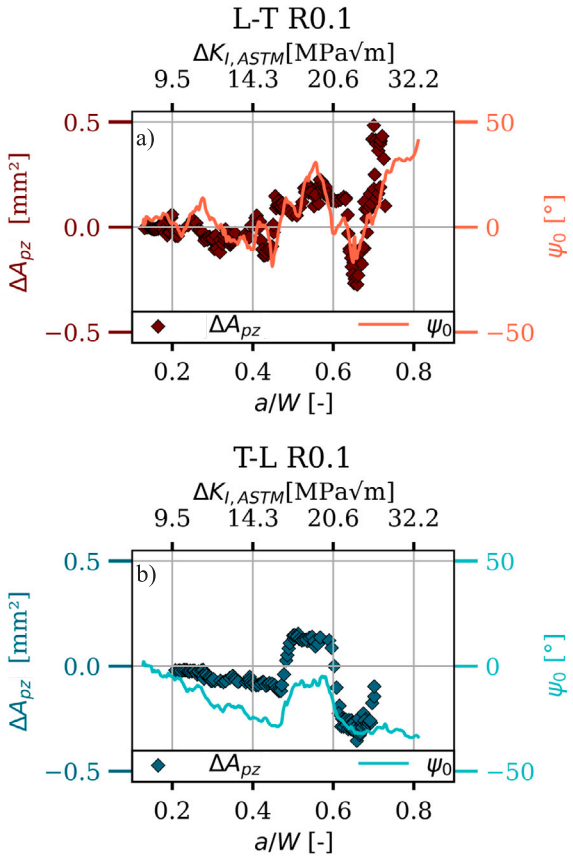

Fig. 19. Comparison of tilt angle ψ_0 and plastic zone area difference ΔA_{pz} for L-T (a) and T-L specimen (b).

of the crack play a crucial role for explaining the $\mathrm{d}a/\mathrm{d}N - \Delta K_{\mathrm{I}}$ differences. Nevertheless, in addition to their remarks regarding the influence of crack deflection and bifurcation, as also previously highlighted by Zheng et al. [37], the authors of this paper also propose that the variations in tilted crack front geometries should be incorporated into the discourse.

The normalized stress intensity factor $K_{II,\psi}$ in Fig. 16 demonstrates that the crack front exhibits a mean value of K_{II} that is nearly zero, indicating that K_{II} is independent of the tilting angle ψ_0. This finding aligns with the experimental observations, as evident in the kink angle curve in Fig. 19(e) and (f). The crack growth was observed to be macroscopically straight in both tests. A higher K_{II} component would have resulted in a notable deflection of the crack, according to [45].

5. Conclusions

Although fatigue crack growth is often modelled in 2D, considering 3D effects becomes significantly more important in current fracture mechanics research. This paper shares this statement by pointing out the strong influence of tilted crack fronts on mode-1 fatigue crack growth behaviour in thin AA2024-T3 sheets. By employing sophisticated digital techniques, including HR-DIC measurements and 3D scanning of fractured surfaces, we demonstrated, both numerically and experimentally, that the three key elements of this paper – the tilted crack front, the plastic zone, and their respective crack propagation curves – are inherently interrelated. In particular, we draw the following conclusions:

- For the first time, the plastic zone during an entire fatigue crack propagation experiment was analysed and correlated with the local crack front geometry. It was demonstrated that the area ratio of the plastic zone on the surface provides valuable insights into the tilting of the crack front. By observing the shape of the plastic zone, it is possible to assess the tilted 3D crack front geometry, despite the fact that only 2D surface information is available. In good agreement between numerical and experimental analyses, a pronounced asymmetry of the plastic zone was observed, which is attributed to the resulting mixed-mode state.
- A comparison of the fracture surfaces of the L-T and T-L fatigue cracks revealed the presence of local differences in the geometry of the crack fronts. By deriving a mapping function that adjust ΔK_{I} to ΔK_{eqv} that takes into account the tilted crack front geometry, we demonstrated that the differences in tilted crack front geometries in L-T and T-L may explain the discrepancies

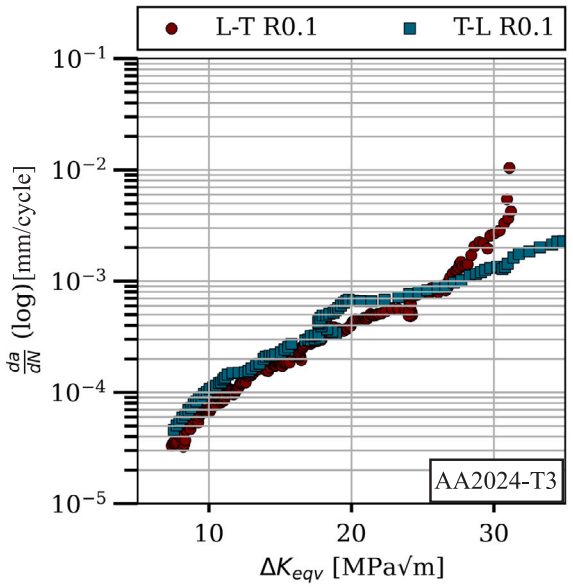

Fig. 20. Comparison of the crack propagation curve $da/dN - \Delta K_{eqv}$ of L-T and T-L oriented specimens, taking into account the local tilt angle in the SIF calculations.

observed in their traditional $da/dN - \Delta K$ crack propagation curves. Both the tilting angle modified crack propagation curves $da/dN - \Delta K_{eqv}$ in L-T and T-L crack orientation exhibit a high degree of superposition.

CRediT authorship contribution statement

Vanessa Schöne: Writing – review & editing, Writing – original draft, Visualization, Methodology, Investigation, Formal analysis, Data curation, Conceptualization. **Florian Paysan:** Writing – review & editing, Data curation, Conceptualization. **Eric Breitbarth:** Writing – review & editing, Supervision, Investigation, Formal analysis, Conceptualization.

Declaration of competing interest

The authors declare that they have no known competing financial interests or personal relationships that could have appeared to influence the work reported in this paper.

Acknowledgements

This work was supported by the Deutsche Forschungsgemeinschaft, Germany (DFG) via the project *Experimental analysis and phase-field modelling of the interaction between plastic zone and fatigue crack growth in ductile materials under complex loading* (grant numbers KA 3309/12-1, BR 6259/2-1). Further support was given by the German Federal Ministry for Economic Affairs and Climate Action (BMWK), Germany through the project ATON embedded in the German aeronautic research fund LuFo 2020–2024 (code 20W1904G).

Data availability

Data will be made available on request.

References

[1] ASTM International. Standard Test Method for Measurement of Fatigue Crack Growth Rates, doi: 10.1520/E0647-15E01.
[2] Schijve J. Fatigue of structures and materials in the 20th century and the state of the art. Int J Fatigue 2003;25(8):679–702. http://dx.doi.org/10.1016/S0142-1123(03)00051-3.
[3] Hohenwarter A, Leitner T, Pippan R. Fatigue crack propagation across the multiple length scales of technically relevant metallic materials. Annu Rev Mater Res 2024. http://dx.doi.org/10.1146/annurev-matsci-080222-101859.
[4] Chowdhury S, Deeb M, Zabel V. Effects of parameter estimation techniques and uncertainty on the selection of fatigue crack growth model. Structures 2019;19:128–42. http://dx.doi.org/10.1016/j.istruc.2018.11.018.

[5] Park H-B, Kim K-M, Lee B-W. Plastic zone size in fatigue cracking. Int J Press Vessels Pip 1996;68(3):279–85. http://dx.doi.org/10.1016/0308-0161(95)00066-6, URL https://www.sciencedirect.com/science/article/pii/0308016195000666.

[6] Chikh BO, Imad A, Benguediab M. Influence of the cyclic plastic zone size on the propagation of the fatigue crack in case of 12NC6 steel. Comput Mater Sci 2008;43(4):1010–7. http://dx.doi.org/10.1016/j.commatsci.2008.02.019.

[7] Benrahou KH, Benguediab M, Belhouari M, Nait-Abdelaziz M, Imad A, Nait-Abdelaziz M, Imad A. Estimation of the plastic zone by finite element method under mixed mode (I and II) loading. Comput Mater Sci 2007;38(4):595–601. http://dx.doi.org/10.1016/j.commatsci.2006.04.001.

[8] Subramanya HY, Viswanath S, Narasimhan R. A three-dimensional numerical study of mixed mode (I and II) crack tip fields in elastic–plastic solids // a three-dimensional numerical study of mixed mode (I and II) crack tip fields in elastic–plastic solids. Int J Fract 2005;136(1–4):167–85. http://dx.doi.org/10.1007/s10704-005-5422-5.

[9] Dugdale DS. Yielding of steel sheets containing slits. J Mech Phys Solids 1960;8.2:100–4.

[10] Besel M, Breitbarth E. Advanced analysis of crack tip plastic zone under cyclic loading. Int J Fatigue 2016;93:92–108. http://dx.doi.org/10.1016/j.ijfatigue.2016.08.013, URL https://www.sciencedirect.com/science/article/pii/S0142112316302468.

[11] Golos K, Wasiluk B. Role of plastic zone in crack growth direction criterion under mixed mode loading. Int J Fract 2000;102(4):341–53. http://dx.doi.org/10.1023/A:1007663728926.

[12] Wasiluk B, Hoshide T, Wasiluk B, Hoshide T. The fracture process in elastic-plastic materials under biaxial cyclic loading. Int J Fatigue 2003;25(3):221–9. http://dx.doi.org/10.1016/S0142-1123(02)00091-9.

[13] Zeinedini A. A novel fixture for mixed mode I/II/III fracture testing of brittle materials. Fatigue Fract Eng Mater Struct 2019;42(4):838–53. http://dx.doi.org/10.1111/ffe.12955.

[14] Gupta M, Alderliesten R, Benedictus R. A review of T-stress and its effects in fracture mechanics. Eng Fract Mech 2015;134:218–41. http://dx.doi.org/10.1016/j.engfracmech.2014.10.013.

[15] Sousa R, Castro J, Lopes A, Martha L. On improved crack tip plastic zone estimates based on T-stress and on complete stress fields. Fatigue Fract Eng Mater Struct 2013;36(1):25–38. http://dx.doi.org/10.1111/j.1460-2695.2012.01684.x.

[16] Uguz A, Martin JW. Plastic zone size measurement techniques for metallic materials. Mater Charact 1996;37(2–3):105–18. http://dx.doi.org/10.1016/S1044-5803(96)00074-5.

[17] Carroll JD, Abuzaid W, Lambros J, Sehitoglu H. High resolution digital image correlation measurements of strain accumulation in fatigue crack growth. Int J Fatigue 2013;57:140–50. http://dx.doi.org/10.1016/j.ijfatigue.2012.06.010, URL https://www.sciencedirect.com/science/article/pii/S0142112312002113. Fatigue and Microstructure: A special issue on recent advances.

[18] Paysan F, Dietrich E, Breitbarth E. A robot-assisted microscopy system for digital image correlation in fatigue crack growth testing. Exp Mech 2023. http://dx.doi.org/10.1007/s11340-023-00964-9.

[19] Camas D, Garcia-Manrique J, Gonzalez-Herrera A. Numerical study of the thickness transition in bi-dimensional specimen cracks. Int J Fatigue 2011;33(7):921–8. http://dx.doi.org/10.1016/j.ijfatigue.2011.02.006.

[20] Kotousov A, Lazzarin P, Berto F, Pook LP. Three-dimensional stress states at crack tip induced by shear and anti-plane loading. Eng Fract Mech 2013;108:65–74. http://dx.doi.org/10.1016/j.engfracmech.2013.04.010.

[21] Paysan F, Breitbarth E. Towards three dimensional aspects of plasticity-induced crack closure: A finite element simulation. Int J Fatigue 2022;163:107092. http://dx.doi.org/10.1016/j.ijfatigue.2022.107092.

[22] Liu H, Yang X, Li S, Shi D, Qi H. Modeling fatigue crack growth for a through thickness crack: An out-of-plane constraint-based approach considering thickness effect. Int J Mech Sci 2020;178:105625. http://dx.doi.org/10.1016/j.ijmecsci.2020.105625.

[23] Zuidema J, Blaauw HS. Slant fatigue crack growth in A1 2024 sheet material. Eng Fract Mech 1988;29(4):401–13. http://dx.doi.org/10.1016/0013-7944(88)90028-8.

[24] Breitbarth E, Strohmann T, Requena G. High–stress fatigue crack propagation in thin AA2024–T3 sheet material. Fatigue Fract Eng Mater Struct 2020;43(11):2683–93. http://dx.doi.org/10.1111/ffe.13335.

[25] Felter CL, Nielsen KL. Assisted crack tip flipping under mode I thin sheet tearing. Eur J Mech A Solids 2017;64:58–68. http://dx.doi.org/10.1016/j.euromechsol.2017.01.009.

[26] Yamada Y, Lacy T, Newman Jr JC, Smith B, Kumar B. Effects of crack closure on fatigue crack-growth predictions for 2024-T351 aluminum alloy panels under spectrum loading. Int J Fatigue 2007;29(8):1503–9. http://dx.doi.org/10.1016/j.ijfatigue.2006.10.026.

[27] Li HF, Qian CF. Experimental study of I + III mixed mode fatigue crack transformation propagation. Fatigue Fract Eng Mater Struct 2011;34(1):53–9. http://dx.doi.org/10.1111/j.1460-2695.2010.01491.x.

[28] Besson J, McCowan C, Drexler E. Modeling flat to slant fracture transition using the computational cell methodology. Eng Fract Mech 2013;104:80–95. http://dx.doi.org/10.1016/j.engfracmech.2013.02.032, URL https://www.sciencedirect.com/science/article/pii/S0013794413000830.

[29] Esnault JB, Doquet V, Massin P. A three-dimensional analysis of fatigue crack paths in thin metallic sheets. Int J Fatigue 2014;62:119–32. http://dx.doi.org/10.1016/j.ijfatigue.2013.03.015.

[30] Mahgoub E, Deng X, Sutton MA. Three-dimensional stress and deformation fields around flat and slant cracks under remote mode I loading conditions. Eng Fract Mech 2003;70(18):2527–42. http://dx.doi.org/10.1016/S0013-7944(03)00082-1.

[31] Dursun T, Soutis C. Recent developments in advanced aircraft aluminium alloys. Mater Des (1980-2015) 2014;56:862–71. http://dx.doi.org/10.1016/j.matdes.2013.12.002.

[32] Bergner F. A new approach to the correlation between the coefficient and the exponent in the power law equation of fatigue crack growth. Int J Fatigue 2000;22(3):229–39. http://dx.doi.org/10.1016/S0142-1123(99)00123-1.

[33] Antunes F, Serrano S, Branco R, Prates P. Fatigue crack growth in the 2050-T8 aluminium alloy. Int J Fatigue 2018;115:79–88. http://dx.doi.org/10.1016/j.ijfatigue.2018.03.020, URL https://www.sciencedirect.com/science/article/pii/S0142112318301129. Crack tip fields 4.

[34] Jian H, Luo J, Tang X, Li X, Yan C. Influence of microstructure on fatigue crack propagation behaviors of an aluminum alloy: Role of sheet thickness. Eng Fract Mech 2017;180:105–14. http://dx.doi.org/10.1016/j.engfracmech.2017.05.038, URL https://www.sciencedirect.com/science/article/pii/S001379441730187X.

[35] Influence of grain structure and crystallographic orientation on fatigue crack propagation behavior of 7050 alloy thick plate. Int J Fatigue 2014;66:55–64. http://dx.doi.org/10.1016/j.ijfatigue.2014.03.009.

[36] Esin VA, François M, Belkacemi LT, Irmer D, Briez L, Proudhon H. Effect of microstructure on fatigue crack deviation in AA2050-T84. Mater Sci Eng A 2022;858:144120. http://dx.doi.org/10.1016/j.msea.2022.144120, URL https://www.sciencedirect.com/science/article/pii/S092150932201499X.

[37] Zheng Z, Cai B, Zhai T, Li S. The behavior of fatigue crack initiation and propagation in AA2524-T34 alloy. Mater Sci Eng A 2011;528(4):2017–22. http://dx.doi.org/10.1016/j.msea.2010.10.085, URL https://www.sciencedirect.com/science/article/pii/S0921509310012633.

[38] Kalina M, Schöne V, Spak B, Paysan F, Breitbarth E, Kästner M. Fatigue crack growth in anisotropic aluminium sheets — phase-field modelling and experimental validation. Int J Fatigue 2023;176:107874. http://dx.doi.org/10.1016/j.ijfatigue.2023.107874.

[39] Johnson HH. Calibrating the electric potential method for studying slow crack growth. Mater Res Stand 1965;(5.1):442–5.

[40] Melching D, Strohmann T, Requena G, Breitbarth E. Explainable machine learning for precise fatigue crack tip detection. Sci Rep 2022;12(1):9513. http://dx.doi.org/10.1038/s41598-022-13275-1.

[41] Strohmann T, Starostin-Penner D, Breitbarth E, Requena G. Automatic detection of fatigue crack paths using digital image correlation and convolutional neural networks. Fatigue Fract Eng Mater Struct 2021;44(5):1336–48. http://dx.doi.org/10.1111/ffe.13433.
[42] Lecompte D, Smits A, Bossuyt S, Sol H, Vantomme J, van Hemelrijck D, Habraken. Quality assessment of speckle patterns for digital image correlation. Opt Lasers Eng 2006;44(11):1132–45.
[43] Zappa E, Mazzoleni P, Matinmanesh A. Uncertainty assessment of digital image correlation method in dynamic applications. Opt Lasers Eng 2014;56:140–51. http://dx.doi.org/10.1016/j.optlaseng.2013.12.016.
[44] Sutton MA, Yan JH, Tiwari V, Schreier HW, Orteu JJ. The effect of out-of-plane motion on 2D and 3D digital image correlation measurements. Opt Lasers Eng 2008;46(10):746–57. http://dx.doi.org/10.1016/j.optlaseng.2008.05.005.
[45] Richard HA, Schramm B, Schirmeisen N-H. Cracks on mixed mode loading – theories, experiments, simulations. Int J Fatigue 2014;62:93–103. http://dx.doi.org/10.1016/j.ijfatigue.2013.06.019.
[46] Schijve J. Shear lips on fatigue fractures in aluminium alloy sheet material. Eng Fract Mech 1981;14(4):789–800. http://dx.doi.org/10.1016/0013-7944(81)90091-6.
[47] Jekel CF, Venter G. Pwlf: A python library for fitting 1D continuous piecewise linear functions. 2019.
[48] Ling MR, Schijve J. Fractographic analysis of crack growth and shear lip development under simple variable–amplitude loading. Fatigue Fract Eng Mater Struct 1990;13.5:443–56.
[49] Tamarin Y. 2nd ed.. Atlas of Stress-strain Curves, ASM International; 2002.
[50] Irwin GR. Analysis of stresses and strains near the end of a crack traversing a plate. 1957, 361–364.
[51] Jia YJ, Shi MX, Zhao Y, Liu B. A better estimation of plastic zone size at the crack tip beyond Irwin's model. J Appl Mech 2013;80(5):051014. http://dx.doi.org/10.1115/1.4023642.
[52] Li H, Chandra N. Analysis of crack growth and crack-tip plasticity in ductile materials using cohesive zone models. Int J Plast 2003;19(6):849–82. http://dx.doi.org/10.1016/S0749-6419(02)00008-6.
[53] Pook LP. A 50-year retrospective review of three-dimensional effects at cracks and sharp notches. Fatigue Fract Eng Mater Struct 2013;36(8):699–723. http://dx.doi.org/10.1111/ffe.12074.